

Reflection imaging of aseismic zones of the Nazca slab by global-phase seismic interferometry

Yohei Nishitsuji¹, Elmer Ruigrok², Martín Gomez³, Kees Wapenaar¹, and Deyan Draganov¹

Abstract

Obtaining detailed images of aseismic parts of subducting slabs remains a large challenge for understanding slab dynamics. Hypocenter mapping cannot be used for the purpose due to the absence of seismicity, whereas the use of receiver functions might be compromised by the presence of melt. Global tomography can be used to identify the presence of the slab, but it does not reveal the structure in detail. We have determined how detailed images can be obtained using global-phase seismic interferometry. The method provides high-resolution (<15 km in depth) pseudo zero-offset (i.e., colocated source and receiver) reflection information. We have applied the method to aseismic zones of the Nazca slab in which initiation of possible slab tearing and plume decapitation was identified by global tomography and electrical conductivity, respectively. We have obtained an image of the Moho and the mantle and found an attenuated area in the image consistent with the presence of an aseismic dipping subducting slab. However, our interpretation was not unambiguous. The results confirmed that the method is useful for imaging aseismic transects of slabs.

Introduction

It has been shown that at the northern part of central Chile (30°S–33°S), the Nazca slab is of the flat type (Rosenbaum et al., 2005; Anderson et al., 2007; Eakin et al., 2014). At that part, the upwelling plume was recently imaged (Booker et al., 2004). Still, the slab's geometry in the southern part of central Chile (34°S–37°S) is unclear and it is unknown whether that part of the slab is not torn (Gilbert et al., 2006; Pesicek et al., 2012).

One of the challenges in imaging the slab in this region by seismological methods relates to the absence of seismicity. Although hypocenter mapping is a useful method for identifying the Wadati-Benioff zone (Cahill and Isacks, 1992; Syracuse and Abers, 2009; Bloch et al., 2014), it cannot be used to image the aseismic region.

The receiver-function method (Langston 1979; Audet et al., 2009; Kawakatsu and Yoshioka, 2011) can be used to image aseismic regions, but so far it has not yielded images of the aseismic zone in this region. Yuan et al. (2000) suggest that the reason for this might be the possible completion of the gabbro-eclogite transformation within the Nazca slab. Gilbert et al. (2006) suggest large attenuation of S-wave energy in the mantle wedge as another possible reason.

Global tomography (Aki et al., 1977; Dziewonski et al., 1977; Boschi and Becker, 2011) is a tool for inves-

tigating global-scale geodynamics and it can be used for imaging aseismic zones. However, the method's resolution (≈ 50 km) poses limitations on estimating the slab's exact location and continuity at local scale, thus leaves a lot of uncertainties.

The reflection method with active sources (explosives, vibroseis, and airguns) provides the needed high-resolution imaging capabilities, but its depth penetration is fundamentally limited by the strength of the sources used.

Here, we demonstrate the usefulness of an alternative seismic technique to image the aseismic slab zone with high resolution, namely, seismic interferometry (SI) for body-wave retrieval (Claerbout, 1968; Scherbaum, 1987a, 1987b; Daneshvar et al., 1995; Wapenaar, 2003) using global-phase SI (GloPSI) (Ruigrok and Wapenaar, 2012). Global phases are seismic phases that travel through the earth's core before reaching the surface. They are induced by earthquakes at epicentral distances greater than 120° (global distances). The global phases are extracted from the continuous field recordings and used as contributions from separate transient sources. For the considered configuration, this is closely related to the work of Kumar and Bostock (2006) and Nowack et al. (2006). For a horizontally layered (1D) acoustic medium, SI retrieves the reflection

¹Delft University of Technology, Department of Geoscience and Engineering, Delft, The Netherlands. E-mail: y.nishitsuji@tudelft.nl; c.p.a.wapenaar@tudelft.nl; d.s.draganov@tudelft.nl.

²Utrecht University, Department of Earth Sciences, Utrecht, The Netherlands and Royal Netherlands Meteorological Institute (KNMI), R&D Seismology and Acoustics, De Bilt, The Netherlands. E-mail: e.n.ruigrok@uu.nl.

³International Center for Earth Sciences, Comisión Nacional de Energía Atómica, Buenos Aires, Argentina. E-mail: mpgomezfw@gmail.com.

Manuscript received by the Editor 30 December 2015; revised manuscript received 14 March 2016; published online 20 May 2016. This paper appears in *Interpretation*, Vol. 4, No. 3 (August 2016); p. SJ1–SJ16, 11 FIGS., 2 TABLES.

http://dx.doi.org/10.1190/INT-2015-0225.1. © 2016 Society of Exploration Geophysicists and American Association of Petroleum Geologists. All rights reserved.

response of the medium from the autocorrelation of the medium's plane-wave transmission response measured at the surface (Claerbout, 1968). GloPSI is a 3D generalization of the mentioned 1D case — it extends the illumination to include a range of ray parameters (horizontal slownesses) allowing retrieval of reflections from 3D structures. At seismic stations, these extra ray parameters would come from the recorded global P-wave arrivals, such as the phases PKP, PKiKP, and PKIKP. Phase names are used as defined in Storchak et al. (2003). These arrivals (phases) have ray parameters lower than 0.04 s/km and are characterized in the mantle by nearly planar wavefronts. This makes these phases suitable for SI by autocorrelation. Due to the autocorrelation, GloPSI retrieves pseudo zero-offset reflection arrivals that penetrate deep enough to allow slab imaging with resolution dictated by the frequency bandwidth of the phases, sensor configuration, and two-way traveltime difference between consecutive arrivals. GloPSI may further shed light on one of the open questions in the geoscience community of whether small deformations and/or detachments (<25 km) are actually present in the slab (Wortel and Spakman, 2000).

In the following, we show how to apply GloPSI to field waveform data. First, we describe the GloPSI method, then we describe the data we use, the phase extraction, and the preparation, and then we show our results and their interpretation. Our results image the aseismic zone of the slab and possible deformation in the slab.

Global-phase SI Theory

The 1D theory from Claerbout (1968) was generalized for a 3D inhomogeneous medium by Wapenaar (2003). Ruigrok and Wapenaar (2012) apply the generalization of SI for retrieval of body waves from the autocorrelation of global phases recorded at seismic stations in Himalaya and Tibet. They call this specific application GloPSI.

The GloPSI relation for the retrieval of the zero-offset reflection response $R(\mathbf{x}_R, \mathbf{x}_R, t)$ for collocated source and receiver at the location of station \mathbf{x}_R is (Ruigrok and Wapenaar, 2012)

$$\sum_{P_{\min}}^{P_{\max}} \sum_{\theta_{\min}}^{\theta_{\max}} \{T(\mathbf{x}_R, \mathbf{p}_S, -t) * T(\mathbf{x}_R, \mathbf{p}_S, t) * E_i(-t) * E_i(t)\} \propto \{\delta(t) - R(\mathbf{x}_R, \mathbf{x}_R, -t) - R(\mathbf{x}_R, \mathbf{x}_R, t)\} * \bar{E}_n(t), \quad (1)$$

where $T(\mathbf{x}_R, \mathbf{p}_S, t)$ is the transmission response (selected global phase) at the receiver location \mathbf{x}_R due to an earthquake i , arriving from direction $\mathbf{p}_S = (p, \theta)$ with ray parameter p and back azimuth θ , $E_i(t)$ is the source time function of the i th earthquake, $\bar{E}_n(t)$ is the average of the autocorrelations of the different source time functions, and $*$ denotes the convolution. In our case, the absolute value of the ray parameter varies between 0 and 0.04 s/km, whereas θ varies between 0° and 360° . In equation 1, the summation is

effectively over plane-wave sources, instead of over point sources. A derivation of the SI relation from point sources to plane-wave sources can be found in Ruigrok et al. (2010). The zero-offset reflection response retrieved by GloPSI can be used to image the subsurface structures in a way similar to the conventional reflection seismic method with active sources. Note that GloPSI directly produces zero-offset reflection responses of the subsurface, which is one of the conventional goals of the active-source reflection method. With the latter, offset measurements are stacked to obtain pseudo zero-offset traces (Yilmaz, 1987) because direct zero-offset measurements are still commercially impractical. A difference between the zero-offset section retrieved by GloPSI and an active-source pseudo zero-offset section is that the virtual source in the former radiates energy vertically and near-vertically down into the earth, whereas in the latter, the pseudo zero-offset source radiates in all directions. Because of this, GloPSI will image horizontal to mildly inclined structures directly, whereas steeply dipping structures will be manifested by a lack of reflections reaching the receivers and can be interpreted by discontinuation of imaged (nearly) horizontal structures. This is similar to the problem in the active-source reflection method, in which a steeply dipping structure lying relatively deep compared with the receiver-array length will not be imaged (Yilmaz, 1987).

When the length of the used receiver array is sufficiently long, relative to the depth of the structure of interest, and given a sufficiently wide illumination (in terms of ray parameters and back azimuths), the autocorrelation in GloPSI relation 1 can be replaced by crosscorrelation, which would permit retrieval of offset reflections as well. This would allow for direct imaging of a broader range of dipping structures.

In Figure 1, we show in a schematic way how GloPSI would (or would not) retrieve reflection responses from four different structural settings.

Comparison with the receiver-function method

The receiver-function method depends on phase conversions (P-to-S or S-to-P) occurring in transmission. GloPSI with P-wave phases uses reflection information and depends only on the P-wave impedance contrasts, just like the conventional reflection method. Comparisons of imaging results from SI and receiver function have shown that SI provides images with resolution at least as high as the receiver-function image (Abe et al., 2007). In cases of structural contrasts that are due to relatively thin layers, SI has the potential to provide higher resolution than the receiver function. For example, suppose there is a mantle structure 5 km below the Moho, which is illuminated by a P-wave phase with an incidence angle of 10° . The P- and S-wave velocities between the structure and the Moho are 8.1 and 4.5 km/s, respectively, whereas above the Moho the respective velocities are 5 and 2.5 km/s. The receivers at the surface would record the P-to-S converted

waves from the two boundaries with a time difference of 0.49 s — the time difference for the propagation of the P- and S-waves between the mantle structure and the Moho. A virtual zero-offset reflection recording, retrieved from GloPSI, would contain two P-wave reflections from the impedance contrasts at the Moho and the mantle structure arriving with a time difference of 1.23 s. In terms of wavelength, assuming a center frequency for P- and S-waves of 0.8 Hz, the two arrivals in the recordings used by the receiver-function method would be 0.39 wavelengths apart. In the retrieved recordings from GloPSI, the two P-wave reflections would be 0.99 wavelengths apart, which would allow for higher resolution.

Thus, although until now SI or GloPSI has not been applied for imaging of aseismic slab zones, these methods have the potential to image such zones with temporal (depth) resolution higher than the one that can be achieved using the receiver-function method.

Data

Study area

Figure 2 shows the location of intermediate-depth earthquakes that have occurred from August 1906 to July 2014 around the Malargüe region (35.5°S), Argentina. The locations are taken from the [U.S. Geological Survey \(2014\)](#) earthquake catalog. There could be more earthquakes actually present than shown in Figure 2 if they are not in the catalog. Note that there are no earthquakes deeper than approximately 200 km. There is also an aseismic spot beneath the Peteroa Volcano. This volcano forms part of the Planchón-Peteroa volcanic complex. We are interested in imaging these aseismic zones, and we achieve this using GloPSI. In Figure 2, the station GO05 of the Chilean National Seismic Network and station C02A of the Talca Seismic Network, which we use later for quality control purposes, are also plotted.

MalARRgüe

We apply GloPSI to data from the MalARRgüe array ([Ruigrok et al., 2012](#)). The array recorded continuously ambient noise and seismicity during 2012 in the Malargüe region, Argentina, to the east of the southern part of central Chile. The array consisted of a patchy subarray PV and an exploration-style 2D T-shaped subarray T with arms TN and TE pointing north and east, respectively (see Figure 3). MalARRgüe used short-period (2 Hz) sensors borrowed from the Program for Array Seismic Studies of the Continental Lithosphere (PASS-CAL) managed by Incorporated Research Institutions for Seismology (IRIS). The PV-array consisted of six irregularly spaced stations labeled PV01–PV06, the TN-array formed a line of 19 stations spaced at 2 km and labeled TN02–TN20, and the TE-array formed a line of 13 stations spaced at 4 km and labeled TE01–TE13.

Figure 3 shows the distribution of the global earthquakes we use to extract phases at the PV- and T-array; the phases are then used as input for GloPSI. The

T-array lies above the beginning of the Nazca's aseismic zone, in which possible slab tearing ([Pesicek et al., 2012](#)) and/or the presence of plume decapitation ([Burd et al., 2014](#)) have been proposed.

Selecting and extracting global phases

We use the vertical-component recordings of the MalARRgüe array for GloPSI. Using the Java version of Windows extracted from event data (JWEED) from IRIS and a reference earthquake catalog from USGS, from the recorded total amount of global earthquakes with $M_w \geq 5.5$, we select 66, 72, and 85 earthquakes for the PV, TN-, and TE-array, respectively (Table 1). We use PKP, PKiKP, and PKIKP phases (epicentral distances $\geq 120^\circ$), which travel through the mantle and core, and arrive at the stations with absolute slowness < 0.04 s/km ([Kennett et al., 1995](#)). We search the phases visually using a window of 900 s, which starts 100 s before the expected arrival of the specific P-wave phase;

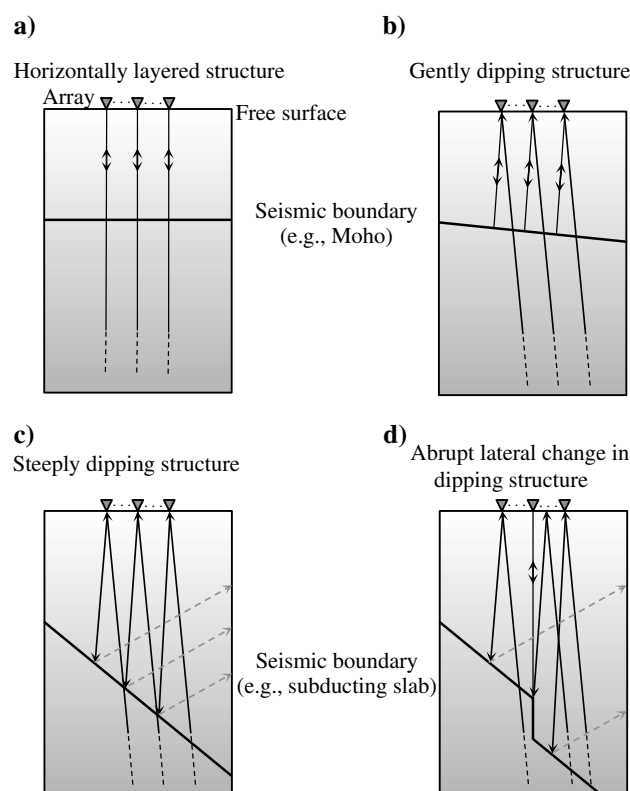


Figure 1. A schematic illustration of how GloPSI would or would not retrieve reflection responses for: (a) a horizontally layered structure and vertical transmission responses; (b) a gently dipping structure and nearly vertical transmission responses; (c) as in panel (b), but for a steeply dipping structure; and (d) as in panel (c), but when an abrupt change (e.g., slab deformation) is present in the lateral continuation of the dipping structure. The black lines indicate the transmission response from the global earthquakes, whereas the gray dashed lines depict the reflection response that will not be recorded at the station due to the configuration. Two-way arrows indicate the reflection response that will be recorded at the station.

we also use as guides the phase pickings that are automatically calculated by IRIS. Then, we extract the desired phases from a shorter window, which is at least

200 s long. This window starts before the arrival of the specific P-wave phase and terminates before onset of the first S-wave phase. Figure 4 shows an example of the windowing.

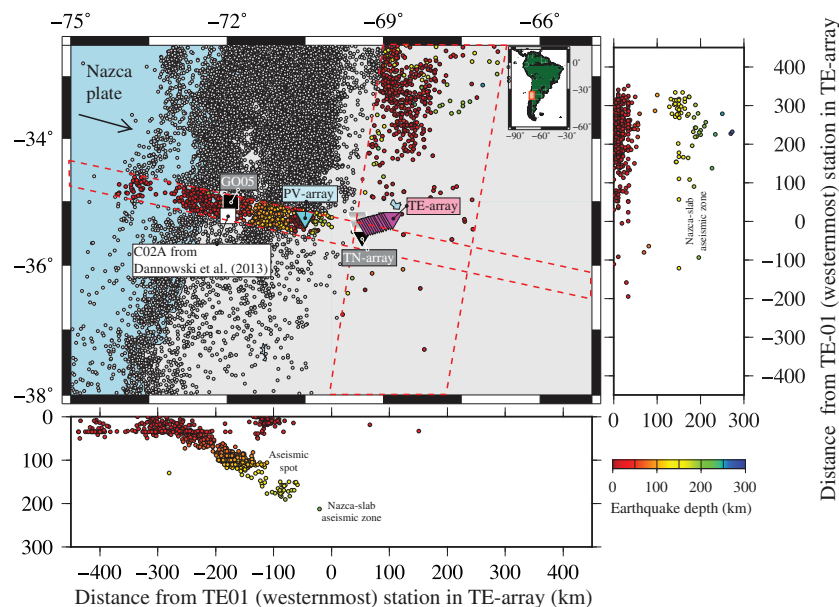


Figure 2. Center: location of the seismic stations used in our study, and hypocenters mapping using earthquakes archived by USGS. Below and right: distribution of the hypocenters in depth within the red dashed line areas in the northwest-southeast-east and north-northeast/south-southwest directions.

For quality control, as described below, we also use data from the station GO05 from the Chilean National Seismic Network, which are situated above the seismic zone of the Nazca slab. For GO05, we use 52 earthquakes recorded by the station during the operation of MalARRgue (Table 1). The complete list of the used earthquakes for MalARRgue and GO05 is given in Table 1.

Data processing Data processing for obtaining images

After deconvolving the recordings with the instrument response, we compute power spectral densities (PSDs) of the global-phase earthquakes to help us select a frequency band that provides adequate signal-to-noise ratio (S/N) of the global phases. Figure 5 shows an example of the computed PSD for earthquakes of different magnitudes higher than 5.5 that occurred at global distances. We select the band 0.3–1.0 Hz using

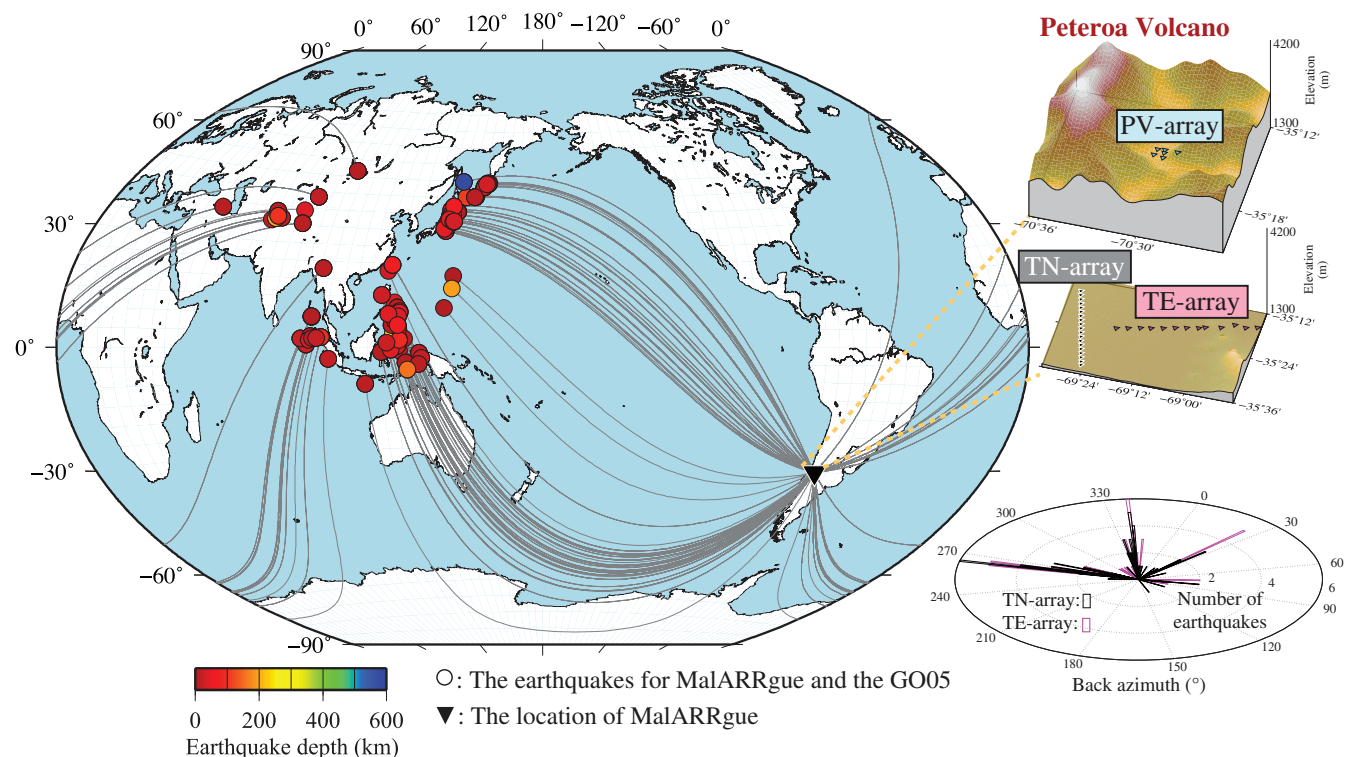


Figure 3. Distribution of the global-phase earthquakes used in our study. The circles show the location of the earthquakes used for MalARRgue and the GO05 station. The location of MalARRgue is indicated by the black triangle with its topography maps (Becker et al., 2009) in the insets. The distribution of the back azimuth of the earthquakes for the T-array is shown in the inset.

Table 1. Global phase seismic used in this study.

Date (day month year)	Time (h:min:s)	Latitude (°N)	Longitude (°E)	Depth (km)	M_w	Array ID
18 January 2012	12:50:21	-0.877	126.829	19	5.7	TE
28 January 12	0:17:11	13.386	124.586	35	5.5	TE
4 February 2012	13:09:23	11.872	125.754	12	5.8	PV/TN/TE/GO
6 February 2012	3:49:13	9.999	123.206	11	6.7	TE
6 February 2012	4:20:00	10.092	123.227	10	5.6	TE
6 February 2012	10:10:20	9.885	123.095	9	6.0	PV/TN/TE/GO
6 February 2012	11:33:37	9.821	123.080	15	5.9	PV/TN/TE/GO
14 February 2012	6:22:01	36.214	141.386	28	5.8	PV/TN/TE/GO
26 February 2012	2:35:01	22.661	120.891	28	5.9	TE
26 February 2012	6:17:20	51.708	95.991	12	6.6	PV/TN/TE/GO
29 February 2012	14:32:48	35.200	141.001	26	5.6	TE
8 March 2012	22:50:08	39.383	81.307	38	5.9	TE
12 March 2012	6:06:41	36.741	73.152	11	5.7	PV/TN/TE
12 March 2012	12:32:46	45.239	147.609	110	5.6	PV/TN/TE
14 March 2012	9:08:35	40.887	144.944	12	6.9	PV/TN/TE
14 March 2012	10:49:25	40.781	144.761	10	6.1	PV/TN/TE
14 March 2012	12:05:05	35.687	140.695	10	6.0	PV/TN/TE
16 March 2012	7:58:02	10.037	125.633	18	5.8	PV/TN/TE/GO
22 March 2012	0:21:37	3.513	125.859	117	5.6	TE
27 March 2012	11:00:45	39.859	142.017	15	6.0	PV/TN/TE/GO
1 April 2012	14:04:25	37.116	140.957	48	5.8	PV/TN/TE
11 April 2012	8:38:37	2.327	93.063	20	8.6	PV/TN/TE/GO
11 April 2012	10:43:11	0.802	92.463	25	8.2	PV/TN/TE/GO
13 April 2012	10:10:01	36.988	141.152	11	5.7	PV/TN/TE/GO
14 April 2012	15:13:14	49.380	155.651	90	5.6	TE
15 April 2012	5:57:40	2.581	90.269	25	6.3	PV/TN/TE/GO
20 April 2012	22:19:47	3.256	93.853	25	5.8	TE
20 April 2012	22:28:59	3.269	93.821	22	5.8	PV/TN/TE/GO
20 April 2012	23:14:31	2.158	93.360	28	5.9	PV/TN/TE/GO
21 April 2012	1:16:53	-1.617	134.276	16	6.7	PV/TN/TE/GO
23 April 2012	21:21:45	0.374	125.293	48	5.7	TE/GO
23 April 2012	22:40:22	48.397	154.739	31	5.7	PV/TN/TE
24 April 2012	14:57:10	8.868	93.949	14	5.6	PV/TN/TE/GO
25 April 2012	7:42:23	9.011	93.945	9	5.9	PV/TN/TE/GO
29 April 2012	8:09:04	2.704	94.509	14	5.7	PV/TN/TE/GO
29 April 2012	10:28:52	35.596	140.349	44	5.8	PV/TN/TE/GO
12 May 2012	23:28:44	38.612	70.354	10	5.7	PV/TN/TE/GO
23 May 2012	15:02:25	41.335	142.082	46	6.0	PV/TN/TE
5 June 2012	19:31:34	34.943	141.132	15	6.1	PV/TN/TE
9 June 2012	14:23:20	48.851	154.852	49	5.5	TE
9 June 2012	21:00:18	24.572	122.248	70	5.9	PV/TN/TE
11 June 2012	5:29:12	36.023	69.351	16	5.7	TE
14 June 2012	20:17:25	1.293	126.828	61	5.5	TE
15 June 2012	1:14:08	5.719	126.354	41	5.7	PV/TN/TE/GO
16 June 2012	22:18:47	15.593	119.563	28	5.9	PV/TN/TE/GO
17 June 2012	20:32:21	38.919	141.831	36	6.3	PV/TN/TE/GO
23 June 2012	4:34:53	3.009	97.896	95	6.1	PV/TN/TE/GO
29 June 2012	21:07:34	43.433	84.700	18	6.3	PV/TN/TE/GO

Table 1. Global phase seismic used in this study. (continued)

Date (day month year)	Time (h:min:s)	Latitude (°N)	Longitude (°E)	Depth (km)	M_w	Array ID
8 July 2012	11:33:03	45.497	151.288	20	6.0	PV/TN/TE
11 July 2012	2:31:17	45.401	151.424	10	5.7	PV/TN/TE
12 July 2012	12:51:59	45.452	151.665	12	5.7	TE
12 July 2012	14:00:34	36.527	70.906	198	5.8	PV/TN/TE
19 July 2012	7:36:35	37.248	71.375	98	5.6	PV/TN/TE/GO
20 July 2012	3:40:12	49.506	155.599	15	5.5	TE
20 July 2012	6:10:25	49.407	155.907	19	6.0	PV/TN/TE/GO
20 July 2012	6:32:56	49.354	156.132	10	5.9	PV/TN/GO
25 July 2012	0:27:45	2.707	96.045	22	6.4	PV/TN/GO
11 August 2012	12:23:18	38.329	46.826	11	6.5	TE
11 August 2012	12:34:36	38.389	46.745	12	6.4	TE
12 August 2012	10:47:06	35.661	82.518	13	6.2	PV/TN/TE/GO
14 August 2012	2:59:38	49.800	145.064	583	7.7	PV/TN/TE
18 August 2012	9:41:52	-1.315	120.096	10	6.3	PV/TN/TE
18 August 2012	15:31:40	2.645	128.697	10	5.8	TE
25 August 2012	14:16:17	42.419	142.913	55	5.9	PV/TN/TE/GO
26 August 2012	15:05:37	2.190	126.837	91	6.6	PV/TN/TE/GO
29 August 2012	19:05:11	38.425	141.814	47	5.5	PV/TN/TE/GO
31 August 2012	12:47:33	10.811	126.638	28	7.6	PV/TN/TE/GO
31 August 2012	23:37:58	10.388	126.719	40	5.6	PV/TN/TE/GO
3 September 2012	6:49:50	6.610	123.875	12	5.9	PV/TN/TE/GO
3 September 2012	18:23:05	-10.708	113.931	14	6.3	PV/TN/GO
3 September 2012	19:44:22	7.905	125.044	10	5.7	PV/TN/TE/GO
8 September 2012	6:54:19	21.527	145.923	5	5.6	TE
8 September 2012	10:51:44	-3.177	135.109	21	6.1	PV/TN/GO
9 September 2012	5:39:37	49.247	155.750	31	5.9	TE
11 September 2012	1:28:19	45.335	151.111	14	5.5	PV/TN/TE/GO
11 September 2012	16:36:50	11.838	143.218	8	5.9	TE
14 September 2012	4:51:47	-3.319	100.594	19	6.3	PV/TN/GO
1 October 2012	22:21:46	39.808	143.099	15	6.0	PV/TN
8 October 2012	11:43:31	-4.472	129.129	10	6.2	PV/TN/GO
12 October 2012	0:31:28	-4.892	134.030	13	6.6	PV/TN/GO
14 October 2012	9:41:59	48.308	154.428	35	5.8	PV/TN
16 October 2012	12:41:26	49.618	156.438	81	5.6	PV/TN
17 October 2012	4:42:30	4.232	124.520	326	6.0	PV/TN
1 November 2012	23:37:18	1.229	122.105	35	5.5	TE
2 November 2012	18:17:33	9.219	126.161	37	6.1	TN/TE/GO
5 November 2012	4:30:27	37.791	143.610	19	5.6	TN/TE/GO
6 November 2012	1:36:22	1.374	122.200	25	5.6	TN/TE/GO
6 November 2012	1:42:26	1.357	122.167	35	5.6	TE
11 November 2012	1:12:39	23.005	95.885	14	6.8	TN/TE/GO
14 November 2012	5:21:42	9.982	122.472	41	5.7	TN/TE/GO
16 November 2012	18:12:40	49.280	155.425	29	6.5	TN/TE/GO
27 November 2012	7:34:25	17.684	145.763	192	5.5	TE
7 December 2012	8:18:23	37.890	143.949	31	7.3	PV/TN/TE/GO
9 December 2012	21:45:35	6.703	126.166	63	5.8	PV/TN/TE/GO
10 December 2012	16:53:09	-6.533	129.825	155	7.1	PV/TN/GO
11 December 2012	6:18:27	0.533	126.231	30	6.0	PV/TN/TE
17 December 2012	9:16:31	-0.649	123.807	44	6.1	PV/TN/TE

a fifth-order Butterworth filter because as in this band all signals of the earthquakes are clearly observed (Figure 5). The lower limit of our band is set at 0.3 Hz due to the low-frequency limitations of the used instruments (Nishitsuji et al., 2014), and to make sure that the double-frequency microseisms noise is largely excluded.

After selecting the frequency band between 0.3 and 1 Hz, we downsample the data from the original sampling of 0.01 to 0.25 s with the aim to minimize the volume of data. After that, we normalize each selected and filtered phase with respect to its maximum amplitude. We also apply despiking to trace intervals with very strong (accidental) signal spikes that saturate the trace for some time (the interval duration). For the TN- and TE-arrays, missing traces at certain stations (e.g., due to despiking) are interpolated using the corresponding records at their neighboring stations (Figure 6).

After the above preprocessing, we apply GloPSI to the selected events for each of the subarrays from MalARRgue (Figure 7). The retrieved zero-offset reflection trace at each station is dominated in the first few seconds by the average autocorrelation convolved with a delta function, $\bar{E}_n(t) * \delta(t)$. To suppress the effect of $\bar{E}_n(t)$, for each subarray we extract the effective source time functions $\bar{E}_n(t)$ from each retrieved zero-offset trace per subarray for a two-way traveltime from 0 to 10 s, take their mean, and subtract the mean from the individual traces in each subarray (Figure 8). This does not cause any changes to signals retrieved later than 10 s, whereas at earlier than 10 s, it preserves the differences between a trace and the mean. The effective source time function of 10 s was selected after testing the above procedure for values from 8 to 13 s with steps of 1 s.

PKP triplication

We also investigate the effect on our results of the PKP triplication (Adams and Randall, 1963) using the T-array. The PKP triplication is expected to arise for earthquakes at epicentral distances from approximately 135° to 155°. The triplicated arrivals are expected within 10 s from the first PKP arrival (Garcia et al., 2004). Each of the PKP triplications will contribute in the autocorrelation process to the retrieval of the same reflections (e.g., from the Moho) and thus would result in an increased S/N of the reflections. For each transmission response, the individual PKP triplicated arrivals will also correlate with each other, which will result in the retrieval of artifacts in the result from each transmission response (crosstalk). However, according to the 3D theory of SI for any inhomogeneous medium, i.e., what we use here, such triplication-related artifacts

will cancel out after summing over the correlated transmission responses (Wapenaar, 2003). Because of this, Ruigrok and Wapenaar (2012) suggest using global

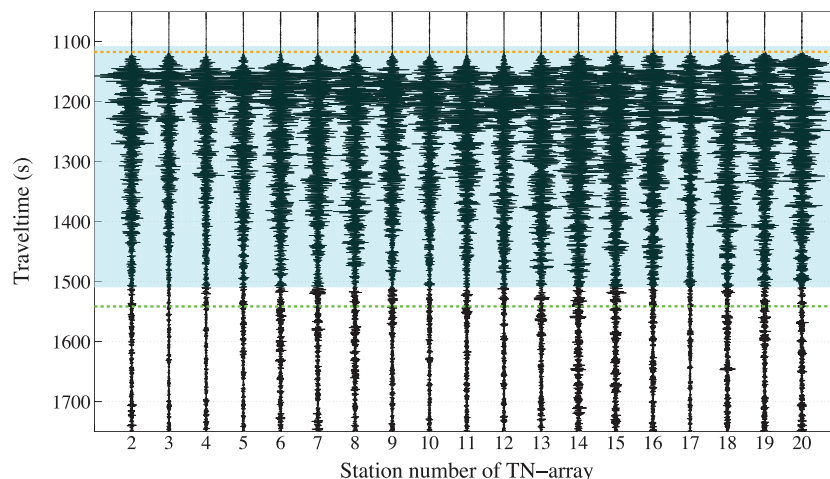


Figure 4. An example recording of a global earthquake on the vertical component of the stations from the TN-array. The area highlighted in light blue indicates the used window that contains the global phases. The orange and green lines indicate the P- and S-wave phase onsets by IRIS, respectively.

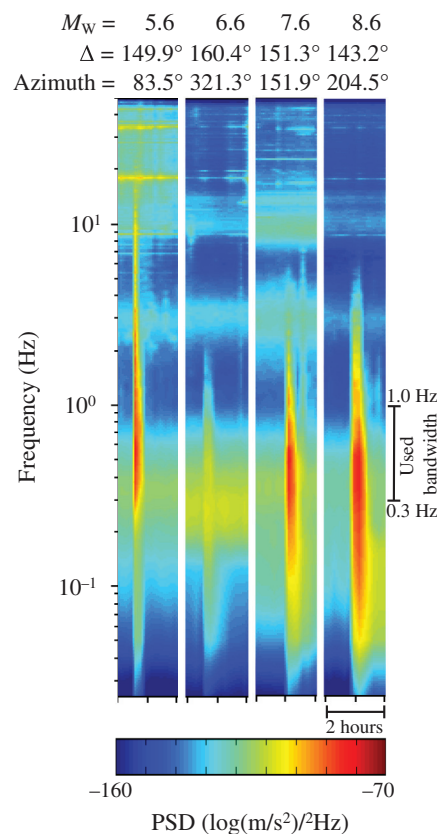


Figure 5. The computed PSDs for four earthquakes with different magnitudes that occurred at global distances. The densities are computed for station TE01 of the TE-array in MalARRgue. The symbol Δ indicates the epicentral distances of the global earthquakes.

phases from a wide range of ray parameters. In the summation process after the autocorrelation, this would cause the different crosstalk artifacts to interact destructively. This happens because the crosstalk artifacts would be retrieved at different times. However, correlations of global phases with a wide azimuthal and slowness coverage enhance the physical arrivals; i.e., the S/N of structures like Moho is improved (Snieder, 2004). In our case, the azimuthal coverage and the slowness variation of the earthquakes with epicentral distances $\geq 120^\circ$ are sufficiently wide (see Figure 3), so we did not exclude the earthquakes that would contain PKP triplications. To the contrary, if we exclude the epicentral distances causing PKP triplication, only 13 earthquakes would remain for both arms of the T-array from the original 72 and 85 earthquakes for the TN- and TE-array, respectively. A reduced number of used earthquakes would result in deterioration of the retrieved reflections from deeper structures.

In Figure 9, we show a comparison of the obtained images of the subsurface when including and excluding

the PKP triplication. When the velocity model of Gilbert et al. (2006) is used for the depth conversion, the top of the Moho is interpreted at a depth of 35 km, whereas the possible effect of the PKP triplication should be seen between depths of 35 and 66 km. The comparison of the results in Figure 9 shows that the Moho in the results when earthquakes with triplications are included is well-imaged without apparent large-amplitude “ringing” around it due to the PKP triplication. In our context, “large” means the amplitude as large as the one of the first Moho reflection, i.e., the reflection at approximately 30 km in Figure 9. There are some slight differences in the weaker amplitude events (e.g., positive-amplitude waveforms approximately 10 km after the Moho reflection), which we attribute to an insufficient integration over the small number of the earthquakes (only 13), when earthquakes with triplications are excluded. Note that the triplication ringing should be present also shallower than the Moho, but there it would be suppressed, even when present, by the subtraction of the averaged source time function $\bar{E}_n(t)$.

The same reasoning for the suppression of crosstalk due to PKP triplication is also valid for the suppression of source-side reverberations — due to differences in the source depths of the different earthquakes, the crosstalk in the autocorrelation between the transmission and the source-side reverberation would be suppressed when summing over the different earthquakes due to destructive interference (Draganov et al., 2004, 2006).

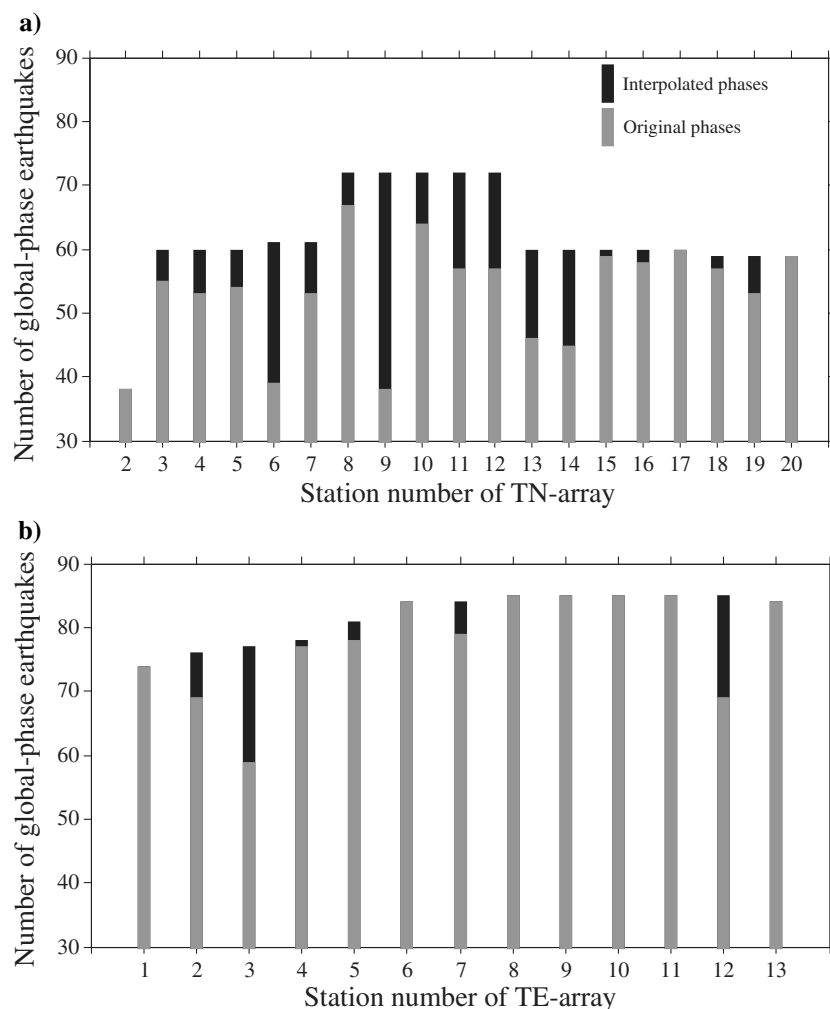


Figure 6. Number of original and interpolated global phases for (a) TN- and (b) TE-array stations.

correct location given an array has a sufficient length. In this study, we apply Kirchhoff poststack time migration (Yilmaz, 1987) to the GloPSI sections from the TN- and TE-arrays. Migration is not applied for the PV-array due to its limited aperture; instead, the individual traces are stacked.

As final processing steps, we apply lateral smoothing along the array to aid the interpretation, using smoothed discretized splines based on the generalized cross-validation (Garcia, 2010) (Figure 10), and then we convert the migrated or stacked traces from time to depth (Figure 11). For the depth conversion, we use a regional velocity model down to a 70 km depth (Gilbert et al., 2006) and the ak135 model (Kennett et al., 1995) to deeper than 70 km.

In Figure 10, we show a comparison of the obtained images when source time functions of 10 and 12 s are used in the estimation of $\bar{E}_n(t)$. It can be seen that the different values give comparable results, which shows the robustness of the procedure. The only substantial difference between the images in Figure 10 is in the interpretation of the top of Moho. When using a

two-way traveltimes of 12 s, it seems that the Moho is largely removed due to its consistent depth over the subarrays. Although it might be possible to improve the time window by taking into account individual source time functions, we found that the constant time window of 10 s is sufficiently effective because we do not see major differences with the result when using a window of 12 s. According to Kanamori and Brodsky (2004), the time window of 10 s covers source time functions for earthquakes smaller or equal to M_w 6.5. Only 8% of the earthquakes used for the TN-array has $M_w > 6.5$.

For the GO05 station, we apply the same processing as for the PV-array, except that during the depth conversion we apply the velocity model as used for the C02A station of the Talca Seismic Network in Dannowski et al. (2013) who use the velocity model of Bohm et al. (2002). An approximation of $\bar{E}_n(t)$ is calculated by taking the average of the retrieved results for GO05 and stations GO04 and GO06, which are the north-south neighbors of GO05 in the Chilean National Seismic Network.

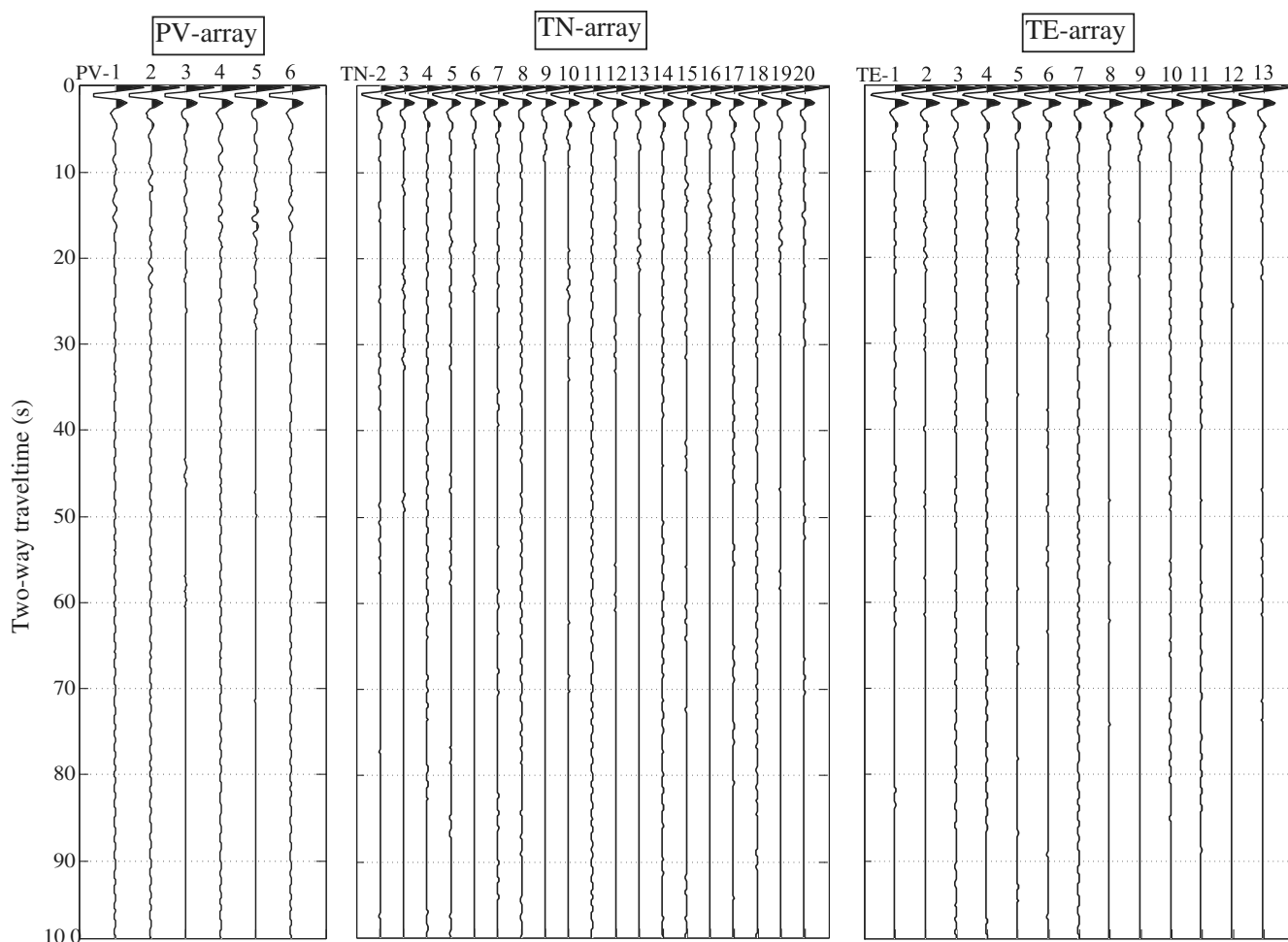


Figure 7. GloPSI results retrieved at the MalARRgue stations before seismic processing. The annotations along the horizontal axis show the actual station codes.

Quality control of the results at the seismic zone of the Nazca slab

For quality-control purpose, we first apply GloPSI to station GO05, which is situated above the seismic zone of the slab. In the processed traces, the peak and trough of the wiggles correspond to depths of P-wave impedance contrasts. We compare the obtained GloPSI zero-offset reflection trace with the receiver-function trace obtained for C02A in [Dannowski et al. \(2013\)](#) (see Figure 11a). From the receiver-function results, [Dannowski et al. \(2013\)](#) estimate the Moho depth at this location at 33 km. GloPSI for GO05 also shows strong amplitude approximately 33 km (Figure 11a). Note that around this depth there starts a cluster of hypocenters (Figures 2 and 11a). Hypocenter clustering delineates the slab, meaning that beneath GO05, the strong positive peaks at depths of approximately 40 and 70 km correspond to the slab's top and bottom, respectively (dashed green lines in Figure 11a). The correspondence of the imaged reflectivity with the hypocenter clustering and also with the slab's bottom from the receiver-function trace (second positive peak at C02A trace in Figure 11a) confirms the validity of applying GloPSI for slab imaging. Imaging reflectivity that is as strong

as the Moho means, that below GO05 the slab is locally (nearly) flat (Figure 1a and 1b). If the slab was locally inclined, the image would have exhibited lack of reflectivity (Figure 1c).

Results interpretation and discussion

Aseismic spot beneath the Peteroa volcano (PV-array)

Similar to the trace for station GO05, beneath the PV-array GloPSI reveals the Moho where the strongest amplitude is seen, that is at a depth of approximately 45 km (Figure 11b). This depth shows good agreement with a recent result of Gravity field and Ocean Circulation Explorer operated by the [European Space Agency \(2014\)](#) (e.g., [Reguzzoni et al., 2013](#)) that shows the Moho depth to be approximately 45 km in this region. A feature further down in the zero-offset reflection trace from the PV-array is the appearance of reflectivity packages at approximately 100 and 150 km depth, where the hypocenters of some intermediate-depth earthquake are present (Figure 11b). Another striking feature is the lack of reflectivity for approximately 15 km around the depth of 125 km. The latter corresponds to an aseismic spot at the Nazca slab. Because of the aseismicity

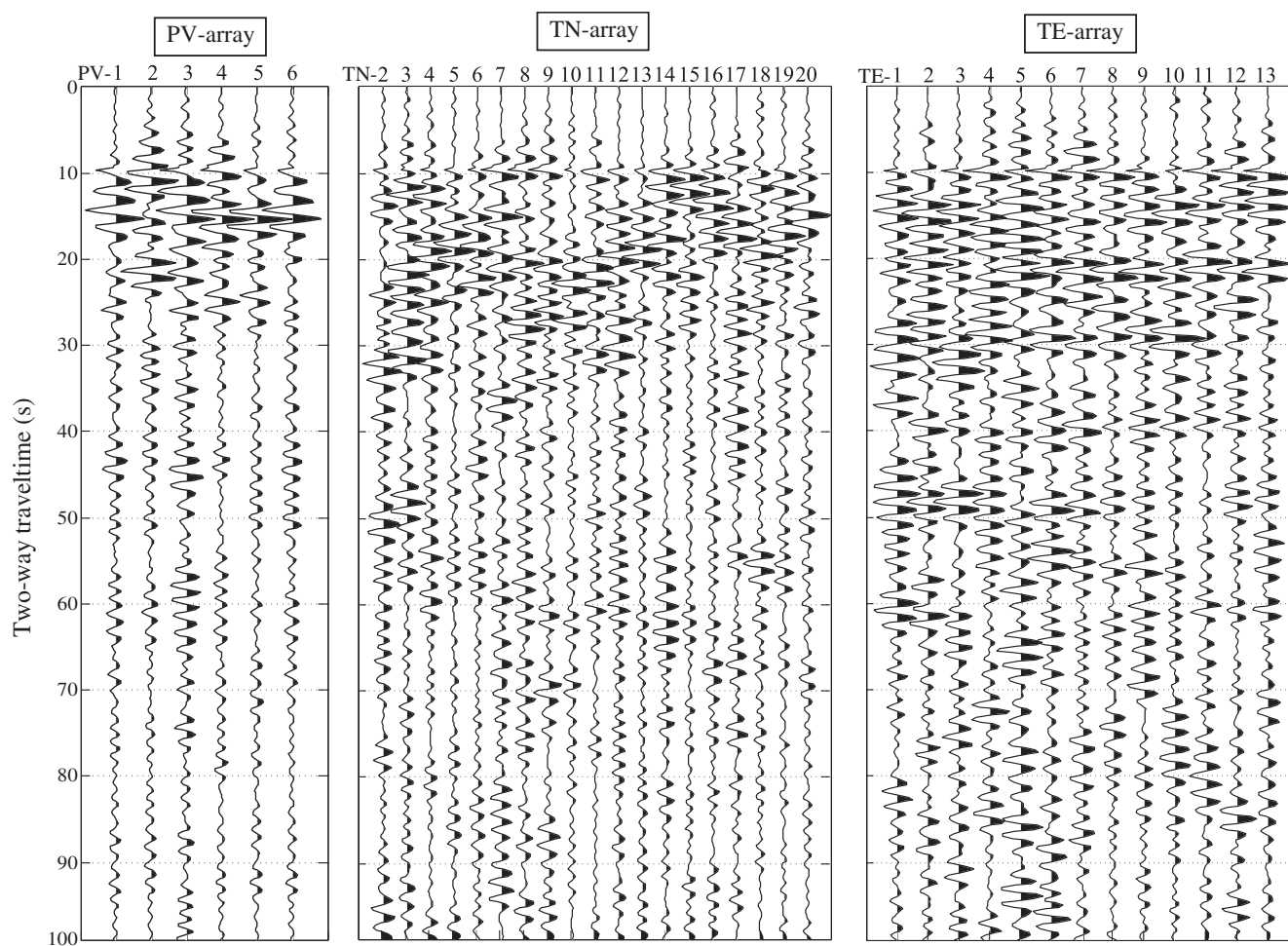


Figure 8. The results from Figure 7 after subtraction of the mean $\bar{E}_n(t)$ per subarray.

and because GloPSI would not image structures where no impedance contrast exists (after applying predictive-deconvolution filter for possible free-surface multiples from the Moho), the lack of reflectivity might be interpreted as being caused by a certain amount of melt. If melted substance is indeed present approximately 125 km depth, then one possible interpretation of the two strong-reflectivity packages at 100 and 150 km depth would be as reflections from slab deformation, which in turn would be caused by the melted substance. The deformation might be in the form of detachment, shearing, necking, or any combination thereof. We illustrate the three pure deformation scenarios in Figure 11d. The present hypocenters indicate vaguely the slab, which is generally characterized as steeply dipping in this zone. The dip would be too steep to retrieve reflections of a dipping interface delineating the slab (Figure 1c), but deformations at the slab would give rise to scattered energy. Some of this energy will be in the form of (nearly) vertically scattered fields, which will be recorded at the station (Figure 1d). The latter will be turned by GloPSI into zero-offset reflections, and consecutively imaged. If the slab is indeed deformed, depending on its thickness (e.g., the transparent green ellipses in Figure 11d), the primary reflection from the top of the slab on one side of the deformation might interfere with the primary reflection from the bottom of the slab from the other side of the deformation, which would make the interpretation of the exact limits of the slab ambiguous. Because of this, in Figure 11b, we indicate with dashed green lines only the extent of the possible deformation of the slab. We interpret the bottom of the slab at approximately 175 km.

Note that if melt is present and forms an impedance contrast with the mantle and/or the slab, GloPSI would retrieve a reflection from this contrast as well unless the melt itself forms a steeply dipping structure (Yilmaz, 1987). However, if there is no or only weak impedance contrast due to, for example, the gabbro-eclogite transformation of the slab, GloPSI will not retrieve a clear reflection from the melt. Frank et al. (2014) show that SI could be applied to S-wave phases as well (e.g., S, SS, ScS, and SKS). S-waves have the advantage that they are more sensitive to melt than P-waves and thus can provide extra information. An implementation of GloPSI to S-wave phases would entail the use of global phases such as PKS and SKS. Such implementation to our temporary deployment would be challenging due to the low S/N on the horizontal components and the attenuation of much of the S-wave phases below the sensitivity bandwidth of the instruments.

We do not exclude other possible interpretations for the lack of reflectivity approximately 125 km. However, our interpretation is a logical consequence of the presence of only a few intermediate-depth earthquakes: The slab here is insufficiently brittle to generate many earthquakes and that might be indicative of a presence of magma with possible slab deformation. Our interpretation is in a good agreement with results from recent

geochemical investigations of Jacques et al. (2013) suggesting that the Planchón-Peteroa complex erupts not only lithospheric magma from the heterogeneous mantle but also magma from the Nazca slab.

Aseismic zone of the Nazca slab beneath the T-array

The migrated images obtained from the results retrieved from GloPSI beneath the TN- and TE-arrays are shown in Figure 11c. With the receiver-function method, Gilbert et al. (2006) interpret an apparently bifurcated Moho, with possibly a magma chamber in between, to be present in this region. Our result shows two strong positive peaks, which appears to confirm the observation of Gilbert et al. (2006). Based on their interpretation, we label the Moho and the magma chamber in Figure 11c in which the trough in blue is imaged at a depth of approximately 40 km. Our GloPSI image shows that the bifurcation is continuous beneath the TN-array, but wedges out to the east beneath the TE-array.

The image of the upper mantle beneath both arms of the T-array reveals a complex structure. This heterogeneous image might correspond to the interpretation of the study of Jacques et al. (2013). In their study, the authors indicate that the mantle wedge in this region

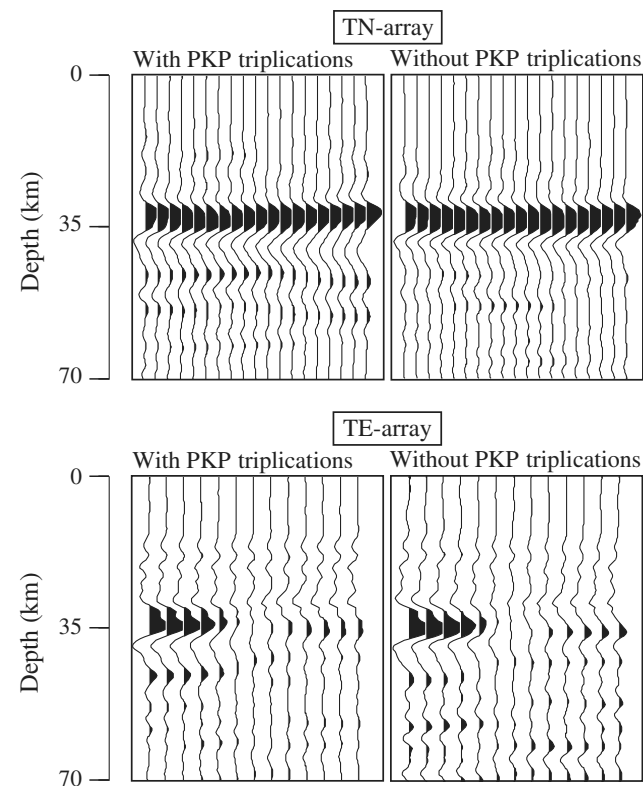


Figure 9. A comparison of GloPSI images obtained when including and excluding global phases with PKP triplications. The number of earthquakes for the TN(TE)-array with and without the PKP triplications are 72 (85) and 13 (13), respectively.

seems to be characterized, from a point of view of geochemical components, by crustal assimilation or mantle heterogeneity. Note that if nonprimary reflections and spurious phases from autocorrelation crosstalk are retrieved, they will contribute to the apparent complexity of the structure. The latter could be caused by source-side reflections (even though we expect such crosstalk to be suppressed by the summation over the different earthquakes), microseismic noise, etc.

Below 100 km, we notice a pronounced discontinuity of the imaged reflectors, indicated by the dashed green line in Figure 11c. This discontinuity is clearly observed below the TN-array from the middle of the array (100 km depth) toward the east (150 km depth). Due to the limited aperture of the T-array, deeper steeply dipping structures will not be imaged, but they will manifest themselves as lack of reflectivity (Figures 4–43 in Yilmaz, 1987). For instance, to record the free-surface multiple of the vertically incident global phase after it is reflected from the Nazca slab characterized by a dip of 40° and depth of 200 km, we need a receiver at the free surface with an offset from the virtual-source position of more than 1000 km (Figure 1c). This can also be said in another way: to retrieve zero-offset reflection from a structure with a dip of 40° , we will need to record incoming phases with incidence angle of 40° as well, which is not possible with global phases. Although some reflection discontinuities may be seen shallower than 150 km, it is difficult to interpret them

without other geophysical information. Note that a longer seismic array would be required to better interpret the mantle structure. Because there is a possible remnant of an upwelling plume in this region (Burd et al., 2014), some of these discontinuities might be related to the plume, but they might also be related to a part of the mantle convection or partial melting.

Let us look at the deeper part of the GloPSI image, where, based on the extrapolation of the mapped hypocenters, we expect to see the Nazca slab. A dimmed-reflectivity zone (between the dashed green lines) is visible beneath the TN-array dipping from north-northwest around a depth of 180–200 km to the south-southeast. This zone causes discontinuity in the strong laterally coherent horizons A and B in Figure 11c. Beneath the TE-array, the GloPSI image exhibits a clear dimmed-reflectivity zone (between the dashed green lines) dipping with an angle of 43° to the east and causing discontinuity in horizon B. Note that horizon B is also visible approximately 62.5 s in Figure 10. The dimmed reflectivity might be caused by lack of impedance contrasts. This, though, would not result in discontinuity of the imaged reflectors. As explained above, another reason for the dimmed reflectivity might be the presence of dipping reflectors, which, because of their depth and the relatively short array length, would not be well-imaged in the (migrated) section (Yilmaz, 1987). The presence of such dipping reflectors would be manifested by discontinuity in horizontal reflectors

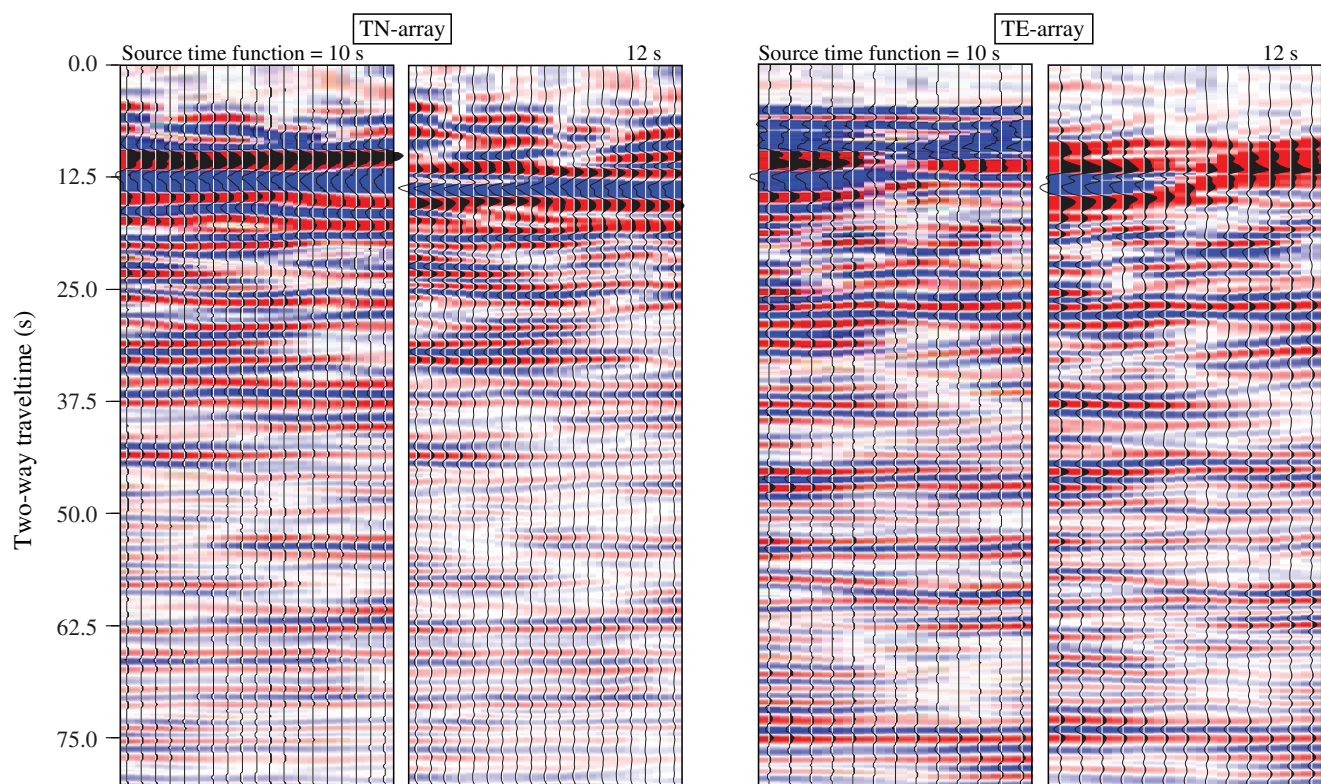


Figure 10. GloPSI results for the TN- and TE-array after poststack time migration with lateral smoothing in the offset orientation when respective source time functions of 10 and 12 s are used in the estimation of $\vec{E}_n(t)$.

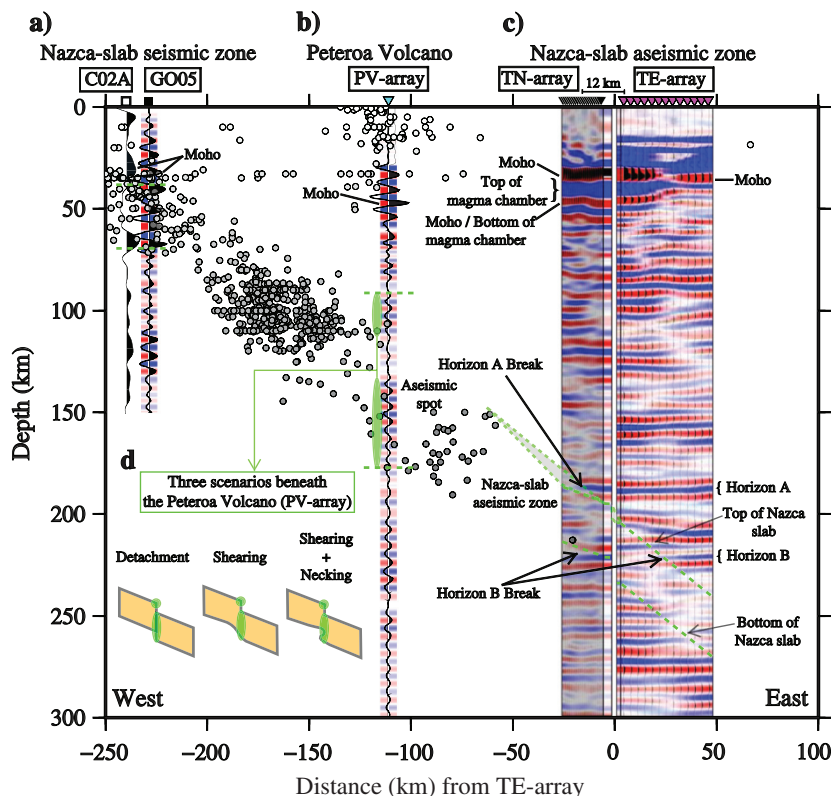


Figure 11. Summarized interpretation with seismicity along the northwest-southeast-east area of GloPSI for MalARRgue and station GO05. (a) GloPSI for GO05 and receiver function for C02A at the Nazca-slab seismic zone. Moho depth is interpreted using receiver function (modified from Dannowski et al., 2013) at C02A. (b) GloPSI for the PV-array beneath the Peteroa volcano. (c) GloPSI for the TN- and TE-array at the Nazca-slab aseismic zone. The dashed green lines in the panels indicate where we interpret the Nazca slab and transparent green rectangles indicate possible interval of the interpretation. The transparent green ellipses indicate where we interpret the Nazca-slab deformation, whereas the transparent gray triangle indicates the possible connection between the Nazca-slab seismic and aseismic zones in three dimensions. The insets in the bottom left corner illustrate three possible scenarios explaining the retrieved strong reflectivity below the PV-array. The gray circles (some transparent for visibility purposes) indicate earthquake hypocenters.

(Figure 11c). That is why, we interpret this dipping dimmed-reflectivity zone as the top and bottom of the aseismic zone of the Nazca slab. We see that this part of the interpreted slab is continuous and that the reflectivity does not indicate a possible slab deformation at this latitude (35.5°S). Because there is no seismicity along this part of the slab, the condition of this steeply dipping slab zone might be different from the condition in the shallower zone where seismicity is present. This might support the interpretation of Yuan et al. (2000) who propose a completion of the eclogite transformation along this part of the slab.

Conclusions

We have presented SI with global phases (GloPSI) for imaging the aseismic and seismic parts of a subducting slab and the mantle above it. GloPSI retrieves reflection responses from coinciding virtual source and

receiver at each seismic station to which it is applied. We applied the method to global P-wave phases recorded by an array of short-period stations installed for one year in the Malargüe region, Argentina, located east of the southern part of central Chile. The array consisted of a station distribution to the east of the Peteroa volcano and two linear subarrays to the east of the town of Malargüe. We processed the retrieved reflection responses to obtain depth images of the subsurface beneath the array. The images to the east of Malargüe town revealed, with high horizontal and vertical resolution, a bifurcated Moho and a complex-structured upper mantle. On the images, we also interpreted the aseismic part of the Nazca slab, which manifested itself as dimmed reflectivity due to the relation between the depth of the dipping reflectors and the short array length we used. The aseismic part of the slab appears to be without tears and to be dipping with an angle of 43° to the east. The image beneath Peteroa also showed the Moho. The deeper part of the image shows packages of strong reflectivity with lack of reflectivity between them. These might be interpreted as a deformation in the dipping slab. If so, the interpreted deformation could be in the form of detachment, shearing, necking, or any combination thereof.

Acknowledgments

The data used in this study were collected using JWEED of IRIS (<http://www.iris.edu/dms/nodes/dmc/>) and a reference earthquake catalog from the USGS (<http://earthquake.usgs.gov/earthquakes/>). This research is supported by the Division for Earth and Life Sciences (ALW) with financial aid from the Netherlands Organization for Scientific Research (NWO) with grant no. VIDI 864.11.009. The research of E. Ruigrok and K. Wapenaar was supported by the Netherlands Research Centre for Integrated Solid Earth Sciences (ISES). The authors thank IRIS-PASSCAL for providing the seismic equipment and the Argentine Ministry of Science, Technology and Production Innovation for the financial support connected to the transportation of the equipment. The authors also thank Pierre Auger Observatory and the Department of Civil Defense of Malargüe for the help during the data acquisition. The authors are thankful to I. Doi at Kyoto University for the fruitful discussion. The authors thank N. Nakata at Stanford University for his constructive comments on an earlier version of the manuscript. The authors also thank S. de Ridder, the assistant special editor, and two anonymous

reviewers for their constructive comments that improved the quality of this manuscript. The maps were drawn with the Generic Mapping Tool (Wessel and Smith, 1991).

References

- Abe, S., E. Kurashimo, H. Sato, N. Hirata, T. Iwasaki, and T. Kawanaka, 2007, Interferometric seismic imaging of crustal structure using scattered teleseismic waves: *Geophysical Research Letters*, **34**, L19305, doi: [10.1029/2007GL030633](https://doi.org/10.1029/2007GL030633).
- Adams, R. D., and M. J. Randall, 1963, Observed triplication of PKP: *Nature*, **200**, 744–745, doi: [10.1038/200744a0](https://doi.org/10.1038/200744a0).
- Aki, K., A. Christoffersson, and E. S. Husebye, 1977, Determination of the three-dimensional seismic structure of the lithosphere: *Journal of Geophysical Research*, **82**, 277–296, doi: [10.1029/JB082i002p00277](https://doi.org/10.1029/JB082i002p00277).
- Anderson, M., P. Alvarado, G. Zandt, and S. Beck, 2007, Geometry and brittle deformation of the subducting Nazca Plate, Central Chile and Argentina: *Geophysical Journal International*, **171**, 419–434, doi: [10.1111/j.1365-246X.2007.03483.x](https://doi.org/10.1111/j.1365-246X.2007.03483.x).
- Audet, P., M. G. Bostock, N. I. Christensen, and S. M. Peacock, 2009, Seismic evidence for overpressured subducted oceanic crust and megathrust fault sealing: *Nature*, **457**, 76–78, doi: [10.1038/nature07650](https://doi.org/10.1038/nature07650).
- Becker, J. J., D. T. Sandwell, W. H. F. Smith, J. Braud, B. Binder, J. Depner, D. Fabre, J. Factor, S. Ingalls, S. H. Kim, R. Ladner, K. Marks, S. Nelson, A. Pharaoh, R. Trimmer, J. Von Rosenberg, G. Wallace, and P. Weatherall, 2009, Global bathymetry and elevation data at 30 arc seconds resolution: SRTM30_PLUS: *Marine Geodesy*, **32**, 355–371, doi: [10.1080/01490410903297766](https://doi.org/10.1080/01490410903297766).
- Bloch, W., J. Kummerow, P. Salazar, P. Wigger, and S. A. Shapiro, 2014, High-resolution image of the North Chilean subduction zone: Seismicity, reflectivity and fluids: *Geophysical Journal International*, **197**, 1744–1749, doi: [10.1093/gji/ggu084](https://doi.org/10.1093/gji/ggu084).
- Bohm, M., S. Lüth, H. Echtler, G. Asch, L. Bataille, C. Bruhn, A. Rietbrock, and P. Wigger, 2002, The Southern Andes between 36° and 40° S latitude: Seismicity and average seismic velocities: *Tectonophysics*, **356**, 275–289, doi: [10.1016/S0040-1951\(02\)00399-2](https://doi.org/10.1016/S0040-1951(02)00399-2).
- Booker, J. R., A. Favetto, and M. C. Pomposiello, 2004, Low electrical resistivity associated with plunging of the Nazca flat slab beneath Argentina: *Nature*, **429**, 399–403, doi: [10.1038/nature02565](https://doi.org/10.1038/nature02565).
- Boschi, L., and T. W. Becker, 2011, Vertical coherence in mantle heterogeneity from global seismic data: *Geophysical Research Letters*, **39**, L20306, doi: [10.1029/2011GL049281](https://doi.org/10.1029/2011GL049281).
- Burd, A. I., J. R. Booker, R. Mackie, A. Favetto, and M. C. Pomposiello, 2014, Three-dimensional electrical conductivity in the mantle beneath the Payún Matrú Volcanic Field in the Andean backarc of Argentina near 36.5°S: Evidence for decapitation of a mantle plume by resurgent upper mantle shear during slab steepening: *Geophysical Journal International*, **198**, 812–827, doi: [10.1093/gji/ggu145](https://doi.org/10.1093/gji/ggu145).
- Cahill, T., and B. Isacks, 1992, Seismicity and shape of the subducted Nazca plate: *Journal of Geophysical Research*, **97**, 17503–17529, doi: [10.1029/92JB00493](https://doi.org/10.1029/92JB00493).
- Claerbout, J., 1968, Synthesis of a layered medium from its acoustic transmission response: *Geophysics*, **33**, 264–269, doi: [10.1190/1.1439927](https://doi.org/10.1190/1.1439927).
- Daneshvar, N. R., C. S. Clay, and M. K. Savage, 1995, Passive seismic imaging using microearthquakes: *Geophysics*, **60**, 1178–1186, doi: [10.1190/1.1443846](https://doi.org/10.1190/1.1443846).
- Dannowski, A., I. Grevemeyer, H. Kraft, I. Arroyo, and M. Thorwart, 2013, Crustal thickness and mantle wedge structure from receiver functions in the Chilean Maule region at 35°S: *Tectonophysics*, **592**, 159–164, doi: [10.1016/j.tecto.2013.02.015](https://doi.org/10.1016/j.tecto.2013.02.015).
- Draganov, D., K. Wapenaar, and J. Thorbecke, 2004, Passive seismic imaging in the presence of white noise sources: *The Leading Edge*, **23**, 889–892, doi: [10.1190/1.1803498](https://doi.org/10.1190/1.1803498).
- Draganov, D., K. Wapenaar, and J. Thorbecke, 2006, Seismic interferometry: Reconstructing the Earth's reflection response: *Geophysics*, **71**, no. 4, SI61–SI70, doi: [10.1190/1.2209947](https://doi.org/10.1190/1.2209947).
- Dziewonski, A. M., B. H. Hager, and R. J. O'Connell, 1977, Large-scale heterogeneities in the lower mantle: *Journal of Geophysical Research*, **82**, 239–255, doi: [10.1029/JB082i002p00239](https://doi.org/10.1029/JB082i002p00239).
- Eakin, C. M., M. D. Long, S. L. Beck, L. S. Wagner, H. Tavera, and C. Condori, 2014, Response of the mantle to flat slab subduction: Insights from local S splitting beneath Peru: *Geophysical Research Letters*, **41**, 3438–3446, doi: [10.1002/2014GL059943](https://doi.org/10.1002/2014GL059943).
- European Space Agency, 2014, www.esa.int/ESA, accessed 26 September 2014.
- Frank, J. G., E. N. Ruigrok, and K. Wapenaar, 2014, Shear wave seismic interferometry for lithospheric imaging: Application to southern Mexico: *Journal of Geophysical Research*, **119**, 5713–5726, doi: [10.1002/2013JB010692](https://doi.org/10.1002/2013JB010692).
- Garcia, D., 2010, Robust smoothing of gridded data in one and higher dimensions with missing values: *Computational Statistics and Data Analysis*, **54**, 1167–1178, doi: [10.1016/j.csda.2009.09.020](https://doi.org/10.1016/j.csda.2009.09.020).
- Garcia, R., S. Chevrot, and M. Webber, 2004, Nonlinear waveform and delay time analysis of triplication core phases: *Journal of Geophysical Research*, **109**, B01306, doi: [10.1029/2003JB002429](https://doi.org/10.1029/2003JB002429).
- Gilbert, H., S. Beck, and G. Zandt, 2006, Lithospheric and upper mantle structure of central Chile and Argentina: *Geophysical Journal International*, **165**, 383–398, doi: [10.1111/j.1365-246X.2006.02867.x](https://doi.org/10.1111/j.1365-246X.2006.02867.x).
- Hansen, R. F., and C. H. Johnson, 1948, Multiple reflections of seismic energy: *Geophysics*, **13**, 58–85, doi: [10.1190/1.1437377](https://doi.org/10.1190/1.1437377).
- Jacques, G., K. Hoernle, J. Gill, F. Hauff, H. Wehrmann, D. Garbe-Schönberg, P. van den Bogaard, I. Bindeman, and L. E. Lara, 2013, Across-arc geochemical variations in

- the Southern Volcanic Zone, Chile (34.5–38.0°S): Constraints on mantle wedge and slab input compositions: *Geochimica et Cosmochimica Acta*, **123**, 218–243, doi: [10.1016/j.gca.2013.05.016](https://doi.org/10.1016/j.gca.2013.05.016).
- Kanamori, H., and E. E. Brodsky, 2004, The physics of earthquakes: *Reports on Progress in Physics*, **67**, 1429–1496, doi: [10.1088/0034-4885/67/8/R03](https://doi.org/10.1088/0034-4885/67/8/R03).
- Kawakatsu, H., and S. Yoshioka, 2011, Metastable olivine wedge and deep dry cold slab beneath southwest Japan: *Earth and Planetary Science Letters*, **303**, 1–10, doi: [10.1016/j.epsl.2011.01.008](https://doi.org/10.1016/j.epsl.2011.01.008).
- Kennett, B. L. N., E. R. Engdahl, and R. Buland, 1995, Constraints on seismic velocities in the earth from travel times: *Geophysical Journal International*, **122**, 108–124, doi: [10.1111/j.1365-246X.1995.tb03540.x](https://doi.org/10.1111/j.1365-246X.1995.tb03540.x).
- Kumar, M. R., and M. G. Bostock, 2006, Transmission to reflection transformation of teleseismic wavefields: *Journal of Geophysical Research*, **111**, B08306, doi: [10.1029/2005JB004104](https://doi.org/10.1029/2005JB004104).
- Langston, C. A., 1979, Structure under Mount Rainier, Washington, inferred from teleseismic body waves: *Journal of Geophysical Research*, **84**, 4749–4762, doi: [10.1029/JB084iB09p04749](https://doi.org/10.1029/JB084iB09p04749).
- Moscoso, E., I. Grevemeyer, E. Contreras-Reyes, E. R. Flueh, Y. Dzierma, W. Rabbel, and M. Thorwart, 2011, Revealing the deep structure and rupture plane of the 2010 Maule, Chile earthquake (M_w 8.8) using wide angle seismic data: *Earth and Planetary Science Letters*, **307**, 147–155, doi: [10.1016/j.epsl.2011.04.025](https://doi.org/10.1016/j.epsl.2011.04.025).
- Nishitsuji, Y., E. Ruigrok, M. Gomez, and D. Draganov, 2014, Global-phase H/V spectral ratio for delineating the basin in the Malargüe region, Argentina: *Seismological Research Letters*, **85**, 1004–1011, doi: [10.1785/0220140054](https://doi.org/10.1785/0220140054).
- Nowack, R. L., S. Dasgupta, G. T. Schuster, and J. M. Sheng, 2006, Correlation migration using Gaussian beams of scattered teleseismic body waves: *Bulletin of the Seismological Society of America*, **96**, 1–10, doi: [10.1785/0120050036](https://doi.org/10.1785/0120050036).
- Pesicek, J. D., E. R. Engdahl, C. H. Thurber, H. R. DeShon, and D. Lange, 2012, Mantle subduction slab structure in the region of the 2010 M8.8 Maule earthquake (30–40°S), Chile: *Geophysical Journal International*, **191**, 317–324, doi: [10.1111/j.1365-246X.2012.05624.x](https://doi.org/10.1111/j.1365-246X.2012.05624.x).
- Reguzzoni, M., D. Sampietro, and F. Sansò, 2013, Global Moho from the combination of the CRUST2.0 model and GOCE data: *Geophysical Journal International*, **195**, 222–237, doi: [10.1093/gji/ggt247](https://doi.org/10.1093/gji/ggt247).
- Rosenbaum, G., D. Giles, M. Saxon, P. G. Betts, R. Weinberg, and C. Duboz, 2005, Subduction of the Nazca ridge and the Inca plateau: Insights into the formation of ore deposits in Peru: *Earth and Planetary Science Letters*, **239**, 18–32, doi: [10.1016/j.epsl.2005.08.003](https://doi.org/10.1016/j.epsl.2005.08.003).
- Ruigrok, E., X. Campman, D. Draganov, and K. Wapenaar, 2010, High-resolution lithospheric imaging with seismic interferometry: *Geophysical Journal International*, **183**, 339–357, doi: [10.1111/j.1365-246X.2010.04724.x](https://doi.org/10.1111/j.1365-246X.2010.04724.x).
- Ruigrok, E., D. Draganov, M. Gomez, J. Ruzzante, D. Torres, I. Lopes Pumarega, N. Barbero, A. Ramires, A. R. Castano Ganan, K. van Wijk, and K. Wapenaar, 2012, Malargüe seismic array: Design and deployment for the temporary array: *The European Physical Journal Plus*, **127**, 126, doi: [10.1140/epjp/i2012-12126-7](https://doi.org/10.1140/epjp/i2012-12126-7).
- Ruigrok, E., and K. Wapenaar, 2012, Global-phase seismic interferometry unveils P-wave reflectivity below the Himalayas and Tibet: *Geophysical Research Letters*, **39**, L11303, doi: [10.1029/2012GL051672](https://doi.org/10.1029/2012GL051672).
- Scherbaum, F., 1987a, Seismic imaging of the site response using microearthquake recordings. Part I. Method: *Bulletin of the Seismological Society of America*, **77**, 1905–1923.
- Scherbaum, F., 1987b, Seismic imaging of the site response using microearthquake recordings. Part II. Application to the Swabian Jura southwest Germany, Seismic network: *Bulletin of the Seismological Society of America*, **77**, 1924–1944.
- Snieder, R., 2004, Extracting the Green's function from the correlation of coda waves: A derivation based on stationary phase: *Physical Review E*, **69**, 046610, doi: [10.1103/PhysRevE.69.046610](https://doi.org/10.1103/PhysRevE.69.046610).
- Storchak, D. A., J. Schweitzer, and P. Bormann, 2003, The IASPEI standard seismic phase list: *Seismological Research Letters*, **74**, 761–772, doi: [10.1785/gssrl.74.6.761](https://doi.org/10.1785/gssrl.74.6.761).
- Syracuse, E. M., and G. A. Abers, 2009, Systematic biases in subduction zone hypocenters: *Geophysical Research Letters*, **36**, L10303, doi: [10.1029/2009GL037487](https://doi.org/10.1029/2009GL037487).
- Syracuse, E. M., and G. A. Abers, 2009, Systematic biases in subduction zone hypocenters: *Geophysical Research Letters*, **36**, L10303, doi: [10.1029/2009GL037487](https://doi.org/10.1029/2009GL037487).
- U.S. Geological Survey, 2014, <http://earthquake.usgs.gov/earthquakes/>, accessed 26 September 2014.
- Wapenaar, K., 2003, Synthesis of an inhomogeneous medium from its acoustic transmission response: *Geophysics*, **68**, 1756–1759, doi: [10.1190/1.1620649](https://doi.org/10.1190/1.1620649).
- Wessel, P., and W. H. F. Smith, 1991, Free software helps map and display data: *EOS Transactions AGU*, **72**, 441–446, doi: [10.1029/90EO00319](https://doi.org/10.1029/90EO00319).
- Wortel, M. J. R., and W. Spakman, 2000, Subduction and slab detachment in the Mediterranean-Carpathian region: *Science*, **290**, 1910–1917, doi: [10.1126/science.290.5498.1910](https://doi.org/10.1126/science.290.5498.1910).
- Yilmaz, Ö., 1987, *Seismic data analysis: SEG*.
- Yuan, X., S. V. Sobolev, R. Kind, O. Oncken, G. Bock, G. Asch, B. Schurr, F. Graeber, A. Rudloff, W. Hanka, K. Wylegalla, R. Tibi, C. Haberland, A. Rietbrock, P. Giese, P. Wigger, P. Röwer, G. Zandt, S. Beck, T. Wallace, M. Pardo, and D. Comte, 2000, Subduction and collision processes in the Central Andes constrained by converted seismic phases: *Nature*, **408**, 958–961, doi: [10.1038/35050073](https://doi.org/10.1038/35050073).



Yohei Nishitsuji received an M.S. (2008) in geophysics from Kyoto University, Japan. He worked at Mitsui Oil Exploration Co. Ltd. for five years as a geophysicist. During this period, he did technical due diligence, seismic processing, and seismic interpretation for the oil and gas assets. He then joined Delft University of Technology (TU Delft) in the Netherlands as a Ph.D. candidate. His project concentrates on the cost-effective seismic investigations including SI. He is a member of SEG and EAGE.



Elmer Ruigrok received a Ph.D. (2012) in geophysics from TU Delft, the Netherlands. He has an education in applied geophysics, but he moved to the field of seismology when applying SI and reflection imaging to naturally induced wavefields. He returned to applied geophysics when developing seismological algorithms for characterizing induced seismicity. Currently, he is a senior seismologist at the Royal Netherlands Meteorological Institute (KNMI) and an assistant professor at Utrecht University. He is a member of SEG, EAGE, AGU, and EGU.

Martín Gomez received a Ph.D. (2012) in science and technology of materials from Universidad de San Martín, Jorge Sabato Institute of Technology, Buenos Aires, Argentina. Since 2004, he has been an assistant professor at National Technologic University (UTN), Argentina and also

works as a scientific director of the International Center of Earth Sciences (ICES), a project belonging to the National Commission of Atomic Energy (CNEA), Buenos Aires, Argentina.



Kees Wapenaar received a Ph.D. (1986) in applied sciences from TU Delft, the Netherlands. At TU Delft, he was an associate professor in the Department of Applied Physics until 1999, when he was appointed as an Antoni van Leeuwenhoek Professor in the Department of Geotechnology. Since 2002, he has been head of the applied geophysics and petrophysics section at that department. His research interests include wave theory and its applications in seismic imaging, multicomponent processing, and seismic interferometric methods. He received SEG's Best Paper in GEOPHYSICS award (2006), the Virgil Kauffman Gold Medal (2010), EAGE's Conrad Schlumberger Award (2013), and he has served as editor-in-chief of GEOPHYSICS from 2007 until 2009. He is a member of SEG, EAGE, AGU, and ASA.

Deyan Draganov received an M.S. (1997) in geophysics from the University of Mining and Geology, Bulgaria, an M.S. (2002) in applied geophysics, and a Ph.D. (2007) in geophysics from TU Delft, the Netherlands. Currently, he is an assistant professor at TU Delft. Since 2005, he has been an associate editor for GEOPHYSICS. In 2010, he received the J. Clarence Karcher Award from SEG. He is a member of SEG and EAGE.